İbrahimcan Görgülü[1]
Department of Mechanical Engineering,
Izmir Institute of Technology,
Izmir 35433, Turkey
e-mail: ibrahimcangorgulu@iyte.edu.tr

Mehmet İsmet Can Dede
Professor
Department of Mechanical Engineering,
Izmir Institute of Technology,
Izmir 35433, Turkey
e-mail: candede@iyte.edu.tr

Giuseppe Carbone
Professor
Department of Mechanical, Energy, and
Management Engineering (DIMEG),
University of Calabria,
Rende CS 87036, Italy
e-mail: giuseppe.carbone@unical.it

Experimental Structural Stiffness Analysis of a Surgical Haptic Master Device Manipulator

This paper deals with haptic devices for master–slave telesurgical applications. Namely, a stiffness model fitting methodology and its fine-tuning are proposed based on experimental results. In particular, the proposed procedure is based on virtual joint structural stiffness modeling to be applied in time-efficient compliance compensation strategies. A specific case study is discussed by referring to the HISS haptic device that has been developed and built at Izmir Institute of Technology. Two different experimental setups are designed for stiffness evaluation tests. Experimental results are discussed to demonstrate their implementation in the proposed methodology for the fine-tuning of stiffness model.
[DOI: 10.1115/1.4049515]

1 Introduction

The use of robotic systems in medical applications includes rehabilitation, training of the surgeon candidates, and surgery procedures [1–3]. Nonautonomous surgical robots are a surgeon on the patient (Surg-on) and surgeon off patient (Surg-off) systems. In Surg-on systems, assistant robots contribute to surgery by holding the tools, preventing the surgeon to approach vital organs, and reducing the effort of the surgeon [4,5]. In Surg-off systems, robots carry out all the surgical procedures while they are controlled by the surgeon/s [6]. Usually, the Surg-off systems are not remotely controlled due to communication delays. However, advancement in communication technologies (i.e., 5G promises lower latency) opens the path to intercontinental robotic surgeries to take place in the near future [7,8].

Remote control of the Surg-off robots only with visual feedback is not sufficient to diagnose if tissue is healthy or not [9]. In addition, the surgeon applies the right amount of force to grasp, cut, and drill in the human tissue in conventional surgery. Therefore, haptic stimuli need to be transmitted between the robot and the surgeon. In this case, the surgical robot (the slave robot) measures forces arising from its interaction with the human tissue and transmits to the human–computer interface (the master haptic robot), to display this information to the surgeon on the surgeon's site [10].

Haptic manipulators should be lightweight for achieving high dynamics performance. However, a lightweight structure exhibits compliant behavior, which is detrimental from an accuracy viewpoint. Figure 1 shows the effect of compliance for a static case when the slave's probe interacts with an object. The desired output force at the knob is computed by making the stiffness of the object K_c and the distance between the pivot (knob) and slave's probe ΔX_c. Note that the pivot position is computed by utilizing encoder data at the actuator and rigid body kinematics. Then, this force is reflected to the operator by the corresponding actuator torque τ_c. Since the actuated arm is flexible and encoders cannot capture this compliant displacement, generated impedance at the knob becomes inaccurate. That is, the operator experiences a larger ΔX_f displacement instead of ΔX_c resulting in a softer K_f stiffness perception of the displayed object.

For an enhanced haptic fidelity, the deformation of flexible bodies must be considered in the computation of haptic information by a stiffness model [11]. This model can be used in the haptic control loop to estimate the end effector location and take the necessary actions [12]. A control loop example that considers the stiffness of the haptic device is given in Fig. 2. The desired force from the remote environment is the force that is aimed to be displayed to the operator. Then, the control loop provides an estimated actual position as the pivot location to the remote environment, which results in more accurate desired impedance generation. In addition, the positioning performance of the slave robot increases since the whole system (Human Operator-Haptic Device-Slave Robot) is coupled through force/position (or force/velocity = impedance). Therefore, slave surgery robot receives accurate position information from the master haptic device, which is crucial for the intended microsurgery applications requiring high accuracy in slave side such as fetal surgery (250 μm),

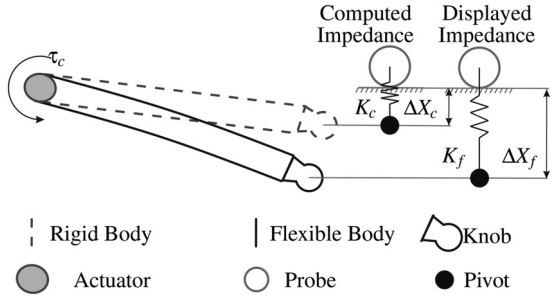

Fig. 1 A simple single arm flexible haptic device

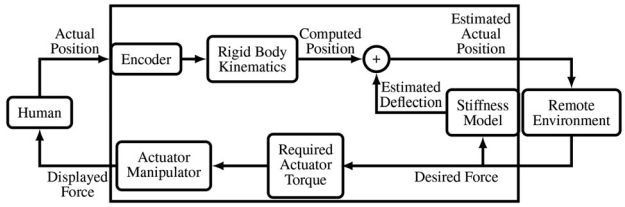

Fig. 2 Haptic control loop

[1]Corresponding author.

Manuscript received September 14, 2020; final manuscript received December 17, 2020; published online February 1, 2021. Assoc. Editor: Nandini Duraiswamy.

vitreoretinal surgery (100 μm), hearing aid implantation (400 μm), vocal cord cordectomy (50 μm), microvascular anastomosis (50 μm), and vasectomy reversal surgery (50 μm) [13].

Finite element analysis (FEA) in stiffness has high accuracy in the cost of long computation time, but an FEA look-up table is used in a real-time application in Ref. [14]. Virtual joint method (VJM) [15] and the matrix structural method (MSM) [16] are proven to be faster in stiffness computation with a minimal loss in the accuracy. For instance, 10 ms computation time for MSM [17], and 0.5 ms computation time for VJM in Ref. [18] are achieved within 1% error range. Still, VJM/MSM models can be modified by FEA results to enhance the accuracy [19].

A haptic device manipulator has several components such as links, bearings, and screws. Also, geometric errors of these parts generate hard to predict internal stresses in parallel manipulators. Considering all these subparts and irregularities in a stiffness model computation is not practical. Therefore, the best approach to obtain an accurate stiffness model is to conduct experimental tests directly on the actual mechanism and modify the obtained stiffness model's parameters following the experimental results. Unfortunately, the literature is focused on industrial manipulators, which are relatively stiffer than the medical robot manipulators. Since the magnitude of haptic interactions is small, the compliant behavior of medical robots is not studied enough.

A review of stiffness analysis and experimental validation of the stiffness model of robotic systems are given in Ref. [20]. In Refs. [21–23] experimental test procedures and design of experiments are described for serial industrial robot manipulators by using laser trackers. In Refs. [24] and [25], stiffness experiments are described for parallel industrial manipulators. In these works, the weights of the links and external forces are considered simultaneously, and the compliant deflections are measured via a dial indicator. In Refs. [26–28], compliant deflections are captured by a camera and computed by using image processing techniques. In Ref. [29], a laser distance sensor is used to measure linear compliant deflections. In Ref. [30], a coordinate measuring machine (CMM) is used to acquire the compliant displacements. In Ref. [31], an experimental setup was designed that measures the compliant deflections indirectly by using linear variable differential transformer sensors. Different from the prior studies, the flexibility of the mobile platform (MP) is taken into account in Ref. [32]. Also, the joint stiffness of industrial serial robots is considered in Ref. [33]. In Ref. [34], linear encoders are attached directly to the MP of the manipulator for measurements. The diversity in all these experiments occurs due to the type of the manipulator to be evaluated, and the used measurement instrumentation [35], but it is common to use calibrated masses to generate external force/torque. The common approach is to conduct several tests to obtain data and fit a stiffness model to the data by adjusting the stiffness parameters, namely, stiffness coefficients of the components.

This paper proposes a new experimental stiffness procedure to address the lack of stiffness investigation of master haptic devices for robotic surgeries. The experiment is easy to conduct and a few kinematic symmetric locations in the workspace are sufficient for measurements. The parameter estimation algorithm does not need a large set of experimental data because it is assisted by a priori FEA data and a compact parameter scaling matrix. We propose two experimental test setups. The first experimental method is based on applying displacement to the MP of the test subject and measuring the reaction force/torque. The setup does not avoid the joint clearance or gravitational effects but it can generate six degrees-of-freedom (DoF) displacements/wrenches. In the second experimental setup, a conventional approach adopted in the literature is used to avoid the joint clearance effects and minimize gravitational effects on the links. Then, the experimental data are utilized to update the VJM stiffness model parameters. Next, a linear model based fine-tuning is applied to compensate for small errors of constant unknown irregularities such as deflections caused by internal stress and the linearization errors of the VJM model. Finally, the modified model is compared with the experimental data. The test subject in this study is a three translational DoF haptic device called HISS [36], which is based on the R-CUBE decoupled parallel manipulator [37]. The manipulator is to be extended to 6DoF by attaching a spherical joint on its MP for the needs of the surgical robots. Stiffness investigation is done in 6DoF space meaning that the experiment procedure is already suitable for higher DoF manipulators.

2 The HISS Haptic Device

In Fig. 3, the HISS haptic device is shown. The actuation system of this prototype is composed of DC motors with capstan drives. There is a balancing spring to compensate for the gravitational load on the actuation system. To discard the stiffness of the actuation system, the rotations of active links are locked with mechanical brakes during the experiments. All metal parts of the links are made of aluminum alloy. The first and the last links in a serial chain are made of carbon fiber hollow tubes to decrease the link's mass. Tubes are assembled with aluminum houses via steel pins and industrial adhesives.

2.1 Kinematic Model of HISS Device. In Fig. 4, a kinematic sketch of the HISS is given. The manipulator has three translational DoF with a decoupled motion structure. $\mathbf{u}_k^{(ij)}$ unit vectors corresponds to orthogonal axes for $k = 1, 2, 3$ and (ij) indicates the jth frame of the ith serial chain. (0) and (p) indicates the fixed and MP frames where $\mathbf{u}_k^{(0)} \parallel \mathbf{u}_k^{(p)}$. $\mathbf{u}_3^{(15)}, \mathbf{u}_3^{(25)}, \mathbf{u}_3^{(35)}$ are aligned with $\mathbf{u}_1^{(35)}, \mathbf{u}_1^{(15)}, \mathbf{u}_1^{(25)}$ vectors, respectively. Note that the dimensions of the MP do not change kinematics of this manipulator since the MP frame is the intersection point of $\mathbf{u}_k^{(p)}$ vectors. The forward kinematics is represented by a single equation as follows:

$$r_i = S + l_1 \sin \varphi_{i1} \quad \text{and} \quad \mathbf{r} = [\, r_1 \quad r_2 \quad r_3 \,]^T \tag{1}$$

where S is the constant distance between the origin and $\mathbf{u}_3^{(i0)}$ and defined as $S = l_1 + d$ where d is the length of a cubic MP. $\mathbf{r}$ is the position vector defining the location of the MP's frame's origin with respect to the origin of the fixed platform's frame. l_1 is a common link length for all the serial kinematic chains' first link. Link lengths are selected as a result of an optimization procedure as $l_1 = 122.3$ mm, $l_2 = 80$ mm, and $l_3 = 129.3$ mm [36]. φ_{i1} is

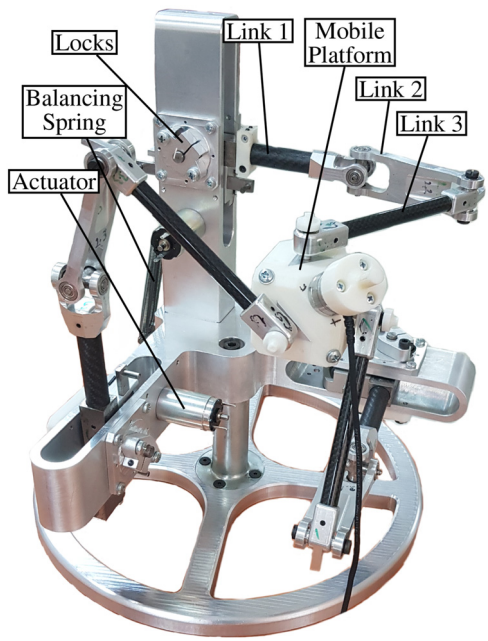

Fig. 3 HISS haptic device

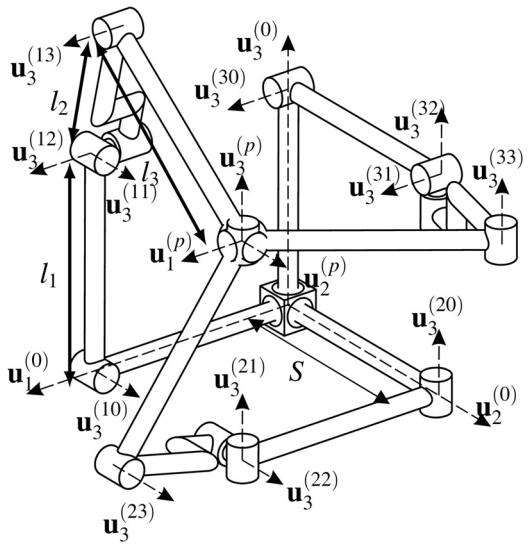

Fig. 4 Kinematic sketch of the HISS [18]

the active joint variable defined about $\mathbf{u}_3^{(i0)}$ and $\varphi_{i1} = 0$ for the given position in Fig. 4. Singularity occurs when $\varphi_{i1} = \pm 90$ deg but, φ_{i1} is limited by ± 30 deg rotation. Joint variable at $\mathbf{u}_3^{(i3)}$ causes singularity when it is 0 deg or ± 180 deg but it is always in negative configuration and ranges between -38 deg and -147 deg.

2.2 Stiffness Model of HISS Haptic Device. An illustration of the VJM model of HISS' single limb is given in Fig. 5. The forward kinematics of the serial chain is formulated via the virtual joint variable vector, $\bar{\boldsymbol{\theta}}_i$, and the regular joint variable vector, $\bar{\boldsymbol{\varphi}}_i$. The passive joint variables of regular joints are isolated in a separate vector $\bar{\boldsymbol{\varphi}}_{pi}$. It is assumed that active joints are rigid. Then, the partial derivative of the forward kinematics is computed to obtain the Jacobian matrices with respect to each variable type as $\mathbf{J}_{\theta i}$ and $\mathbf{J}_{\varphi pi}$. By using these matrices, the compliant deformation of joint space $(\Delta\bar{\boldsymbol{\theta}}_i, \Delta\bar{\boldsymbol{\varphi}}_{pi})$ and task space $(\Delta\bar{\mathbf{X}}_i)$ is related as follows:

$$\Delta\bar{\mathbf{X}}_i = \mathbf{J}_{\theta i}\Delta\bar{\boldsymbol{\theta}}_i + \mathbf{J}_{\varphi pi}\Delta\bar{\boldsymbol{\varphi}}_{pi} \tag{2}$$

$$\Delta\bar{\boldsymbol{\theta}}_i = \mathbf{J}_{\theta i}^{-1}\Delta\bar{\mathbf{X}}_i - \mathbf{J}_{\theta i}^{-1}\mathbf{J}_{\varphi pi}\Delta\bar{\boldsymbol{\varphi}}_{pi} \tag{3}$$

Then, the local stiffness matrix of virtual joints, $\mathbf{K}_{\theta i}$, and the stiffness of passive joints, $\mathbf{K}_{\varphi pi} = \mathbf{0}$ are defined. Next, the external force vector, $\bar{\mathbf{F}}_{i,\text{ext}}$ is mapped to joint space via the Jacobian matrices. In the final form, force/compliant displacement relation is formulated as follows:

$$\begin{bmatrix} \mathbf{J}_{\theta i}^T\bar{\mathbf{F}}_{i,\text{ext}} \\ \mathbf{J}_{\varphi pi}^T\bar{\mathbf{F}}_{i,\text{ext}} \end{bmatrix} = \begin{bmatrix} \mathbf{K}_{\theta i} & \mathbf{0} \\ \mathbf{0} & \mathbf{K}_{\varphi pi} \end{bmatrix} \begin{bmatrix} \mathbf{J}_{\theta i}^{-1}\Delta\bar{\mathbf{X}}_i - \mathbf{J}_{\theta i}^{-1}\mathbf{J}_{\varphi pi}\Delta\bar{\boldsymbol{\varphi}}_{pi} \\ \Delta\bar{\boldsymbol{\varphi}}_{pi} \end{bmatrix} \tag{4}$$

Since $\mathbf{K}_{\varphi pi} = \mathbf{0}$ is valid in an ideal case, the above expression is rewritten in block matrix form

$$\begin{bmatrix} (\mathbf{J}_{\theta i}\mathbf{K}_{\theta i}^{-1}\mathbf{J}_{\theta i}^T) & \mathbf{J}_{\varphi pi} \\ \mathbf{J}_{\varphi pi}^T & \mathbf{0} \end{bmatrix} \begin{bmatrix} \bar{\mathbf{F}}_{i,\text{ext}} \\ \Delta\bar{\boldsymbol{\varphi}}_{pi} \end{bmatrix} = \begin{bmatrix} \Delta\bar{\mathbf{X}}_i \\ \bar{\mathbf{0}} \end{bmatrix} \tag{5}$$

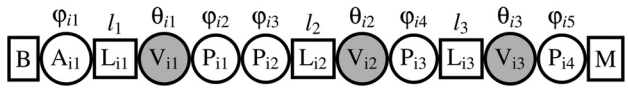

Fig. 5 Compliant kinematics of *i*th limb and its virtual joint model where A is active joint, P is passive joint, V is virtual joint, M is the mobile platform, B is base, L is a link element

The matrix at the left-hand side of Eq. (5) is a compliance matrix of the virtual and passive joints, namely, $\mathbf{C}_i$. Taking the inverse of this matrix produces a rank deficient stiffness matrix. This rank deficiency is a result of passive joints' zero-stiffness effect. The inversion is shown as follows:

$$\mathbf{C}_i = \begin{bmatrix} (\mathbf{J}_{\theta i}\mathbf{K}_{\theta i}^{-1}\mathbf{J}_{\theta i}^T) & \mathbf{J}_{pi} \\ \mathbf{J}_{pi}^T & \mathbf{0} \end{bmatrix} \Rightarrow \mathbf{C}_i^{-1} = \begin{bmatrix} \mathbf{K}_{i[6\times 6]} & \sim \\ \mathbf{K}_{pi} & \sim \end{bmatrix} \tag{6}$$

where upper-left 6×6 subpart of the above inversion contains the desired Cartesian stiffness matrix of *i*th serial chain, $\mathbf{K}_i$. $\mathbf{K}_{pi}$ gives the relation between the compliant deflections and passive joint motion. All serial chains are parallel connected to each other; hence, the stiffness matrix of the manipulator, $\mathbf{K}_C$, is computed by, $\mathbf{K}_C = \sum_{i=1}^{n}\mathbf{K}_i$.

Link 2 is a body composed of a uniform material; hence, FEA produces accurate results for this link. Stiffness of links 1 and 3 are obtained experimentally by hanging masses and measuring the resulting displacements via a CMM. Preliminary results indicated that the stiffness behavior of links 1 and 3 closely resemble the theoretical stiffness of carbon fiber hollow tubes. This indicates that other parts practically have no contribution to its compliance. Therefore, the theoretical stiffness of the hollow tubes is modified by means of experimentally obtained elasticity modulus. The stiffness matrices of the links (those will serve as our initial guesses in the model fitting) are given in the Appendix.

Virtual joint method is based on small compliant displacement assumptions so that it can be used in a real-time control loop since it is fast and reliable. If the forces are high or the manipulator is highly flexible, then, "small displacement assumption" cannot be made anymore. Yet, the VJM can still be used through an iterative computation method where small displacements are addressed at each iteration to cover the whole large displacements. In Section 3, two loading states of the manipulator are defined as before and after external loading, and the VJM model is linearized for zero-loading state. These states can also be defined for each computation step such that the VJM model is linearized depending on the state of the previous and current computation step of the computer, excluding the zero-loading state. The VJM is linearized with respect to its previous iteration step, while the final value of the VJM model output is acquired considering 3 to 5 computation steps [38]. Usually, a haptic control loop runs at 1 kHz of frequency [39]. In our recent study [18], we have shown that our VJM model can run at 2 kHz frequency, which enables the possibility of an iterative approach also in real-time.

3 The Proposed Methodology for Tuning the Model Parameters

The model fitting procedure is described in this section. A flowchart is given to summarize the steps of the proposed approach as follows:

(1) Construct a stiffness model
(2) Formulate an error function
(3) Construct a scaling weight matrix
(4) Minimize the error by adjusting the weight matrix
(5) Fine-tune the model via a correction function

In the initial state, when there is no external input on the end effector, the actual position of the end effector in Cartesian space is computed as follows:

$$\bar{\mathbf{X}}_A^{(1)} = \bar{\mathbf{X}}_R^{(1)} + \bar{\mathbf{X}}_G^{(1)} + \bar{\mathbf{X}}_I^{(1)} + \bar{\mathbf{X}}_J^{(1)} \tag{7}$$

where superscripts denote the state number. $\bar{\mathbf{X}}$ is devoted to the end-effector position information. $\bar{\mathbf{X}}_A$ is the actual location with respect to the inertial frame used for the absolute measurements.

$\bar{\mathbf{X}}_R$ is the position computed via rigid body forward kinematics. $\bar{\mathbf{X}}_G$ is the compliant deflection due to gravitational loads. $\bar{\mathbf{X}}_I$ denotes the compliant deflection caused by internal stresses. Finally, $\bar{\mathbf{X}}_J$ represents the effect of the joint clearance on the position.

When an external force is applied on the end effector, it is transformed into a second state shown as follows:

$$\bar{\mathbf{X}}_A^{(2)} = \bar{\mathbf{X}}_R^{(2)} + \bar{\mathbf{X}}_G^{(2)} + \bar{\mathbf{X}}_I^{(2)} + \bar{\mathbf{X}}_J^{(2)} + \mathbf{K}_C^{-1}\bar{\mathbf{F}} \tag{8}$$

where $\bar{F}$ is the external force vector. The compliant deflection of the end effector that is caused by the external force is computed by the difference of both states.

3.1 Assumptions. To facilitate the methodology and carry out an engineering approach to the problem, a number of assumptions are made. Since the control loop is responsible for regulating the stiffness of the actuators, the compliance behavior due to actuator stiffness is neglected. Thus, $\Delta\bar{\mathbf{X}}_R = \mathbf{0}$. For minimal changes, the variation of gravitational effects can be neglected. Therefore, $\Delta\bar{\mathbf{X}}_G = \mathbf{0}$. Also, we can assume the compliant deflections due to internal stress is minimal if the parallel manipulator is not an overconstrained one and thus, $\Delta\bar{\mathbf{X}}_I = \mathbf{0}$. The joint clearance effect is minimal since the inspected manipulator has a constrained architecture being a parallel manipulator and it has preloaded bearings at its joints to minimize the joint clearance effects, $\Delta\bar{\mathbf{X}}_J \approx \mathbf{0}$. Still, some errors might be observed since the manipulator has a decoupled motion capability, which reduces the internal stresses that might eliminate joint clearances. To solve this problem, successive external forces should be applied in the negative or positive region of the motion axes. As a result, the compliant displacement caused by the external forces and the relation of compliant displacements are given as follows:

$$\Delta\bar{\mathbf{X}} = \bar{\mathbf{X}}_A^{(2)} - \bar{\mathbf{X}}_A^{(1)} = \mathbf{K}_C^{-1}\bar{\mathbf{F}} \tag{9}$$

3.2 Evaluation Process of the Experimental Data. After experimentally obtaining the external forces, $\bar{\mathbf{F}}$, and the compliant displacement, $\Delta\bar{\mathbf{X}}$, $\mathbf{K}_C$ stiffness matrix is to be determined. The nonlinear structure of $\mathbf{K}_C$ is known; hence, the only remaining unknown is the parameters of $\mathbf{K}_{\theta i}$. These parameters are determined such that $\mathbf{K}_C$ complies with the experimental force/displacement relation.

HISS manipulator has three limbs and three links in each limb. Three links in a limb form a symmetric positive definite stiffness matrix that has a size of 18×18. Since all limbs are identical, acquiring a single $\mathbf{K}_\theta$ matrix for all limbs is sufficient. Although $\mathbf{K}_C$ is proportional to $\mathbf{K}_\theta$, direct estimation of $\mathbf{K}_\theta$ via model fitting algorithms is difficult due to the number of parameters. An unambiguous initial value can be assigned to $\mathbf{K}_\theta$ that is close to the actual ones. We propose to construct this initial stiffness matrix by carrying out FEA and/or experiments on each distinct link. FEA is suitable for unibody links. If the link has composite materials and/or subassemblies in its structure, it is advisable to obtain its stiffness matrix experimentally. After defining an initial $\mathbf{K}_\theta$, its divergence from its initial value is computed. To determine the divergence, an unknown diagonal square weighting matrix, $\mathbf{W}$, is inserted in the formulation. In this way, the model fitting algorithm seeks a suitable $\mathbf{W}$ that minimizes the errors between the model and the experiment data. The size of this matrix is the same as $\mathbf{K}_\theta$. The formulation is given as follows:

$$\mathbf{K}'_\theta = \mathbf{W}\mathbf{K}_\theta\mathbf{W}^T \tag{10}$$

where $\mathbf{K}'_\theta$ is generated by the model fitting algorithm.

The elements of $\mathbf{W}$ must be greater than 0 to preserve the positive definiteness of $\mathbf{K}_\theta$. If the first guess of $\mathbf{K}_\theta$ is accurate, then, $\mathbf{W}$ becomes an identity matrix. Since the initial value of $\mathbf{K}_\theta$ is obtained via FEA/experimentally, it is logical to set the initial values of $\mathbf{W}$ to 1. Generally, these elements result between 1 and 0 after the fitting procedure because generally, the actual manipulator has lower stiffness than the theoretical one [25]. Still, there may not be a unique $\mathbf{W}$. If a link does not experience displacement and load along some certain axes or if the link is relatively very stiff along some axes such that applied forces practically do not affect displacement, then it is possible to compute several $\mathbf{W}$ that produces the same displacement values at the end effector. A cost function is defined as follows:

$$E = \sum_1^m \bar{\mathbf{e}}^T\mathbf{L}\bar{\mathbf{e}}, \quad \text{and,} \quad \bar{\mathbf{e}} = \left(\sum_{i=1}^n \mathbf{K}_i\right)^{-1}\bar{\mathbf{F}}^{\exp} - \Delta\bar{\mathbf{X}}^{\exp} \tag{11}$$

where e is the error vector, E is a scalar cost function computed for m many measurements, and $\mathbf{L}$ is the error weighting matrix. The superscript exp denotes that the data are experimentally obtained. $\mathbf{L}$ can be chosen as an identity matrix or can be adjusted to increase the error cost of a certain part of the stiffness matrix. For stiff manipulators, small disturbances or measurement errors in compliant displacements may generate extreme forces when they are multiplied with the stiffness matrix. To avoid this, we have multiplied the inverse of stiffness with the force vector. This makes the cost function more robust to measurement errors.

Next, the number of factors of the weighting matrix, $\mathbf{W}$, is determined. There are three different links each having a 6×6 stiffness matrix. Therefore, there exist 18 variables for a diagonal $\mathbf{W}$. The first stiffness elements of link 1, link 2, and link 3 (given in the Appendix) correspond to tension/compression stiffness and show relatively high stiffness with respect to the other components of the stiffness model. Thus, a weighting factor of 1 is assigned because this element has no noticeable effect on the manipulator's compliance. Second-third and fifth-sixth pair elements on the diagonals of link 1 and link 3 are the same due to the hollow tube structure. Therefore, a single weighting variable can be assigned for each pair. Thus, 11 variables for the diagonal $\mathbf{W}$ are defined in vector form as follows:

$$\bar{\mathbf{W}}^T = [1W_1W_1W_2W_3W_3|1W_4W_5W_6W_7W_8|1W_9W_9W_{10}W_{11}W_{11}] \tag{12}$$

This proposed approach reduces significantly the number of parameters to be identified to 11 parameters while the general case would have required the identification of 63 parameters consisting of all the entries in the three symmetric link stiffness'. It is worth noting that such a high number of parameters would be not suitable for estimation with any model-fitting algorithm unless there is an accurate initial guess value. Also in such a case, significant numerical errors can be foreseen due to the high number of parameters to be identified. Accordingly, our proposed approach promises a quicker and more robust parameter estimation with a minimal experimental dataset.

3.3 Model Fine-Tuning. It is highly possible that model output and experiment data are not fully correlated because the model is an ideal model that does not consider the irregularities in the manipulator. However, modeling each irregularity is not practical. Besides, the stiffness model is constructed on the small displacement assumption meaning that high-compliant deflections cannot be computed accurately. This is presented in our previous work [18] in which FEA and VJM deflections are compared and observed that FEA can compute for larger deflections, unlike VJM. Also, the precision and accuracy of the measurement devices are always limited, thus, a perfect fit is not possible. Yet, the performance of the model can be increased by fine-tuning the stiffness model's outputs.

To fine-tune a model, first, the correlation of the experimental data and model outputs is investigated as shown in Fig. 6 for an example dataset. y axis indicates the experiment data and x axis

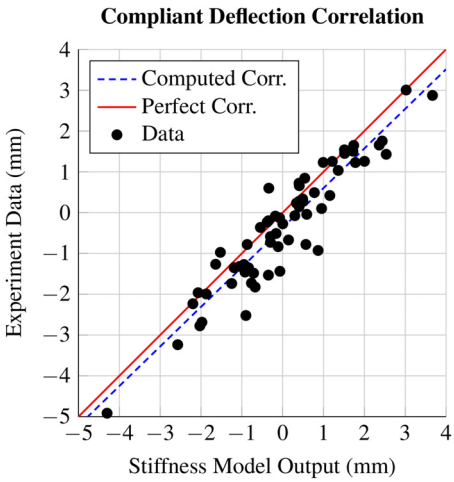

Fig. 6 Experiment data and stiffness model output correlation

shows the stiffness model outputs. If there is a perfect fit between the model output and the experiment data, all computed/measured data should be aligned on a perfect correlation line which has a function of $y = x$. It is not possible to modify the experiment data since it is the ground truth, but the stiffness model output can be processed to make it more correlated with the experiment data. To achieve this, a first-degree function, $x' = ax + b$, is computed to find a computed correlation line as shown in the figure. Here, x' denotes the scaled compliant deflection, a and b are the scaling factor and bias term, respectively. This scaling increases the correlation between the model outputs and experiment data by modifying x to x'. When RMS error values are computed for the given data in Fig. 6, RMS errors before and after scaling are 0.634 and 0.513, respectively.

One may wish to fit a higher degree and nonlinear function for a better result. However, there is a risk of overfitting the model outputs to the experiment results. To preserve the generality of the model, this scaling function must be a lower degree function, preferably linear.

4 HISS Case Study

4.1 Experimental Setup. The workspace of HISS is cubic and symmetric with respect to a diagonal vector of the cube. Therefore, the manipulator shows the same stiffness behavior at several locations. 10 critical and unique locations are determined by the characteristics of the stiffness matrix, i.e., its maximum/minimum determinant [18]. These points are named as TP1, TP2,…, TP10. The experiments are conducted at these locations but three extra measurement points are included as additional checkpoints for diversity. The locations of these 13 points are defined in terms of active joint variables in Table 1.

Two experimental setups are described. The first test setup forces compliant displacements on the manipulator's MP. Meanwhile, a 6-axis force/torque sensor is used for measuring the resulting reaction force/torques. Due to the input–output relationship of this test setup, it is named as displacement/force setup or shortly D/F. The second test setup is configured to apply force/torque on the MP of the manipulator. The resulting compliant displacements are measured. Due to the input–output relationship of this test setup, it is called force/displacement setup, or in short F/D.

Table 1 Experiment test points given by active joint values in degrees, test point (TP)

TP	φ_{11}	φ_{21}	φ_{31}	TP	φ_{11}	φ_{21}	φ_{31}
TP1	−30	−30	−30	TP8	+30	−30	+30
TP2	0	0	0	TP9	+30	−30	+30
TP3	+30	+30	+30	TP10	0	−30	+30
TP4	0	0	+30	TP11	−30	0	+30
TP5	0	0	−30	TP12	−30	0	0
TP6	0	+30	+30	TP13	−30	30	0
TP7	0	−30	−30				

4.2 Displacement/Force Experimental Setup. A gantry-type (GT) manipulator is used in this test setup along with a CMM. The setup and the HISS haptic device are shown in Fig. 7. The GT manipulator has three translational DoF. Each axis of the GT manipulator has a screw-nut system to convert the rotational input to linear end-effector motion. Thanks to the screw-nut system, the system is not back drivable and can be controlled manually.

The MP of HISS is coupled with the end effector of the GT manipulator. The GT manipulator forces the MP of HISS to perform compliant displacements. Consequently, reaction forces/torques occur. The structure of the GT manipulator is designed to be highly rigid so that required compliant displacements can be conveniently displayed on the test subject. A 6-axis force/torque (F/T) sensor is placed in between the MP of HISS and the end effector of the GT manipulator. This connection is achieved via a fixture that has three-dimensional printed fixtures as shown in Fig. 8. The three-dimensional printed components are produced with the maximum material density for rigidity.

The fixture comprises lower/upper parts, the MP, a 6-axis F/T sensor, a sensor connection part, and a spherical joint. One end of the force/torque sensor is attached to the upper part while the other end is fixed to the sensor connection part via screws with a torque adjustable screwdriver. In this way, the stress on the sensor is distributed evenly.

The lower/upper parts wrap the MP of HISS and form a shape-locked sandwich structure. The tightening screws are added to ensure the rigidity of the assembly. The lower part contains 15 semicircular holes in which their locations are known with respect to the MP frame. The holes are used as measurement locations for

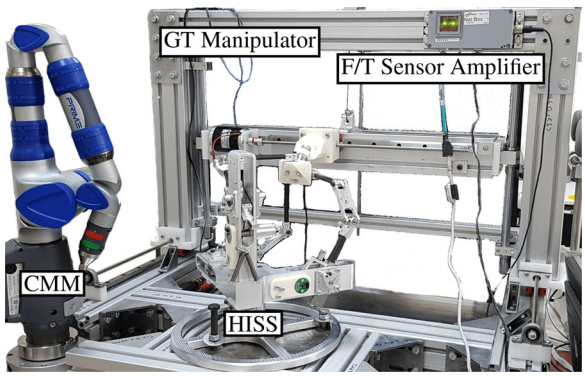

Fig. 7 Displacement/force experimental setup

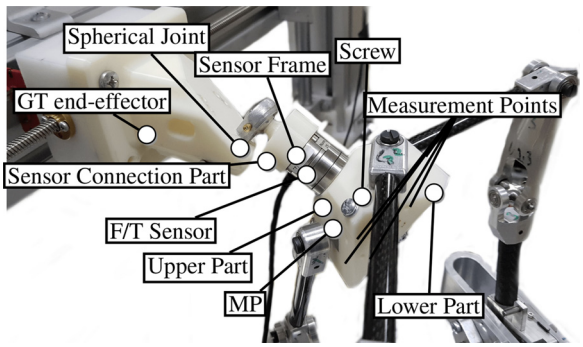

Fig. 8 Displacement/force setup fixtures

CMM's probe and their diameters are compatible with the probe diameter of the CMM. These measurement points are not always reachable for some test point poses due to the HISS-CMM collision. Redundancy in reference points helps us to perform the measurements at all test poses (TPs) of HISS. At each test pose of HISS, when three different hole locations are measured, they form a circle and a plane in space. The center of the circle and the orientation of the plane provide the necessary and sufficient information to determine the MP's translational and rotational deflections.

The sensor connection part is mounted on the end effector of the GT manipulator via a spherical joint. This spherical joint compensates for the angular misalignment between the manipulators. Therefore, there is no internal stress generated as a result of the HISS-GT manipulator assembly.

The benefit of such an experimental setup is that the desired compliant displacements can be exactly displayed on the test subject. The best assembly mode is when the motion axes of HISS-GT manipulator pair align. However, this alignment is not achievable for our manipulators due to the collisions of HISS and GT structures. Therefore, generating displacement along a decoupled motion axis of the HISS is difficult. Besides, rotational compliant displacements always occur since the fixture connection forms a moment arm. Also, it is possible to observe no reaction force/torque for a small deflection region, especially during the transition from negative motion direction to the positive motion direction of HISS motion axes. Nonetheless, we did not observe any significant dead-region effect caused by joint clearances. Consequently, the proposed test setup is foreseen to introduce complexities during the acquisition and processing of the experimental data.

The steps of the test procedure are as follows:

(1) Release the brakes of the active joints of the HISS.
(2) Position the MP at a test point via driving the GT manipulator.
(3) Reset the 6-axis F/T sensor (remove bias offset).
(4) Lock the active joint shafts of HISS without introducing any reaction force/torque.
(5) Use the CMM to measure the position MP by using three measurement holes on the lower fixture.
(6) Move the system via driving the GT manipulator to result in the desired compliant displacements on the HISS.
(7) Use CMM to measure the new position of the MP through the same measurement holes and record the force sensor readings.

In this experimental procedure, all of the TPs of the HISS in Table 1 are used. In each TP, five different compliant displacements are induced to HISS via the GT manipulator. The compliant displacements are given such that the resulting force/torque is different in magnitude and direction in each TP, and also, F/T sensor readings are below 10 N for forces and 0.5 N·m for torques not to damage the HISS manipulator. Including the zero-displacement state, a total of six measurements are performed for each TP; hence, 78 measurement results are acquired in total. However, compliant displacements are computed with respect to the zero-displacement state; hence, five compliant displacement data are computed for each TP resulting in 65 data in total.

4.3 Experimental Setup 2: F/D. F/D test setup addresses the problems of the D/F setup with a conventional approach. The experimental setup is presented in Fig. 9. In this setup, the HISS manipulator's base frame is reoriented to align the diagonal vector of the MP's frame and the gravity vector. An extension platform, named as the mass platform, is attached to the MP to house the calibrated masses. In between, there is a 6-axis F/T sensor. The mass platform has three sockets for the masses. The socket in the middle is used to display forces. The other two sockets are placed at known distances to generate a moment about the origin of the MP's frame.

In this test setup, the weights of the links are equally distributed among the limbs due to this orientation. Also, calibrated mass

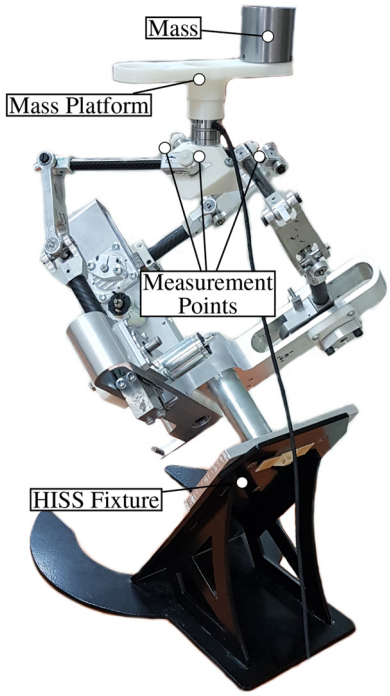

Fig. 9 Force/displacement experimental setup

weights are applied along the negative direction of the diagonal axis of the MP frame to minimize the joint clearance effect. Due to the collision issues of CMM and HISS, new measurement holes are placed on the last revolute joints of the limbs and they are coincident with the axes of the MP. A drawback of the setup is that the probe of the CMM must touch to the measurement points. This may exert additional forces and may cause compliant displacement. Hence, the measurements must be carefully taken.

The steps of the test procedure are given as follows:

(1) Position the MP to a test pose
(2) Reset the 6-axis F/T sensor (remove bias offset)
(3) Lock the active joint shafts
(4) Use CMM for position measurements of MP
(5) Apply external force/torque by placing the calibrated masses on the mass platform
(6) Use CMM to measure the deflected position of the MP through the same measurement holes

In the experiments carried out with the setup, the first 10 TPs in Table 1 is used. In each TP, measurements are carried out in three different loading conditions. In the first two conditions, 0.5 kg and 1 kg masses are placed on the middle socket to avoid any external

Table 2 Weight parameters of model fitting

	D/F		F/D		D/F + F/D	
$\bar{W}$	Fit	Variance	Fit	Variance	Fit	Variance
W_1	0.884	0.197	0.003	0.000	2.123	113.2
W_2	0.038	0.000	0.052	0.000	3.650	2.450
W_3	0.941	0.030	3.954	2.056	6.467	272.3
W_4	0.991	0.000	0.947	0.015	1.029	6.117
W_5	0.866	0.009	3.457	3.786	0.004	0.000
W_6	0.258	0.003	19.46	77.27	0.165	0.000
W_7	0.977	0.226	0.021	0.000	1.534	59.04
W_8	0.978	0.000	1.139	0.247	0.994	33.93
W_9	0.054	0.001	55.50	916.5	0.043	0.000
W_{10}	0.020	0.000	0.035	0.000	0.034	0.000
W_{11}	0.125	0.148	0.074	0.000	0.066	0.000

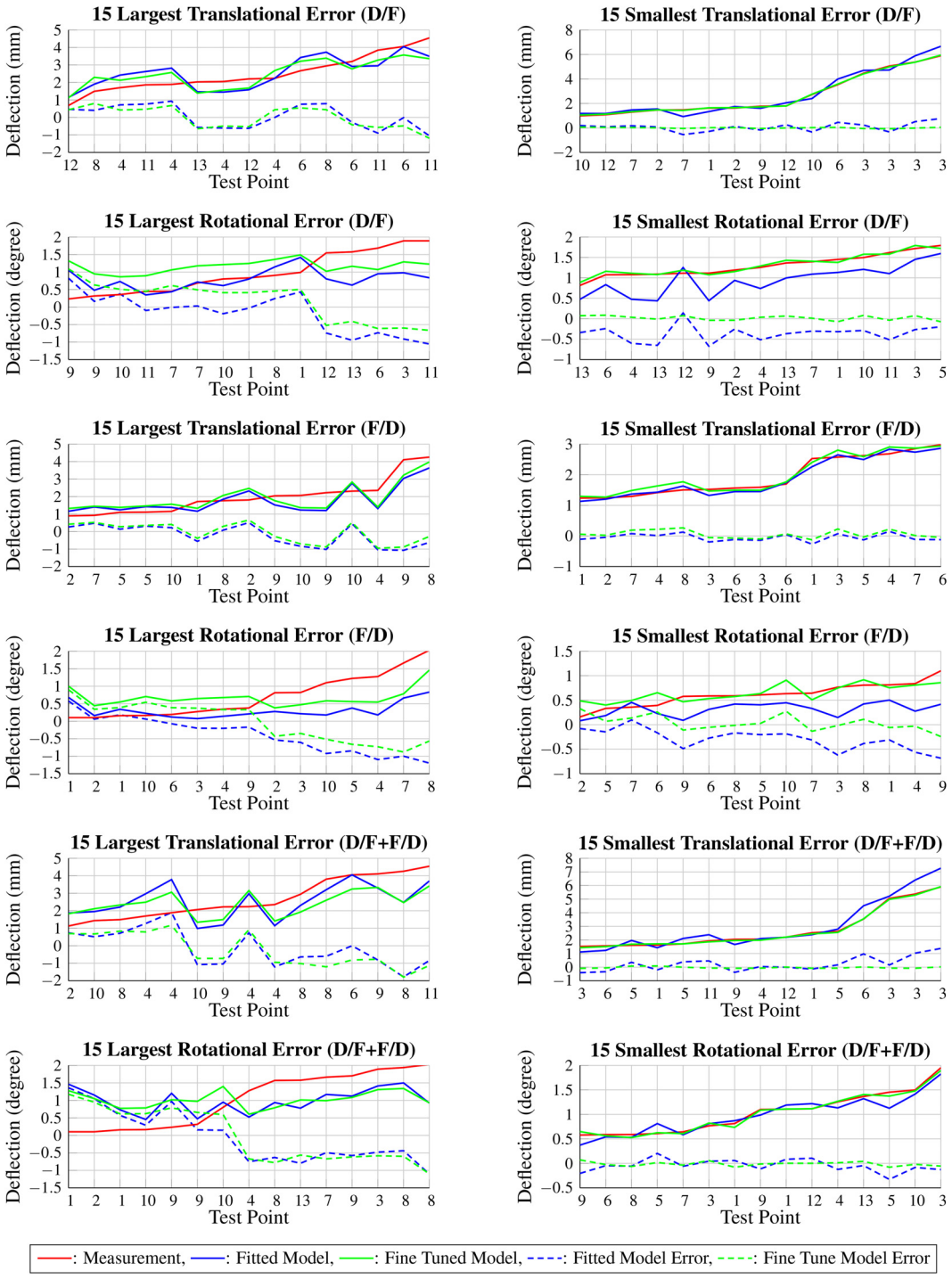

Fig. 10 Top 15 largest and smallest fine-tuned model errors

moments. In the third condition, 0.5 kg mass is placed on one of the side sockets to generate external moments along with the external force. Including the no-added-mass condition, four measurements are carried out for each TP. 30 experiment data are obtained when the compliant displacements are computed with respect to the no-added-mass condition.

5 Stiffness Model Fitting and Fine-Tuning

5.1 Computed Weights for Model Parameters. Experimental data are used to compute the weight matrix **W** by a fitting algorithm. Each dataset is investigated separately and also, together. Thus, three fitting computations are conducted for D/F, F/D, and D/F + F/D (combined). *fminimax* command in MATLAB is adopted to minimize the cost function. Several model fitting runs are conducted. Some weight coefficients are converged to a specific constant while the other ones resulted in different values in each run. This indicates that converged values play an important role in the stiffness model. The top five best fitting **W** determined from D/F, F/D, and D/F + F/D model fitting computations. Then, the variance between the parameters is investigated to determine the insignificant parameters. A set of weight parameters and the variances are shown in Table 2. The weight with a greater variance than 0.1 is considered as insignificant.

As shown in Table 2, W1, W7, and W_{11} have the high variance for D/F fitting. On the other hand, the largest variances are observed on W_3, W_5, W_6, W_8, and W_9 parameters for F/D fitting.

Table 3 Correction function parameters for $\Delta' = a\Delta + b$

	D/F		F/D		F/D + D/F	
	a	*b*	*a*	*b*	*a*	*b*
Δ_x	0.883	0.017	0.956	0.037	0.784	−0.125
Δ_y	0.970	−0.369	1.086	−0.131	0.885	−0.346
Δ_z	0.863	0.014	1.396	0.625	0.778	0.011
Δ_α	0.914	0.328	0.348	0.157	0.627	0.185
Δ_β	1.102	−0.190	1.219	−0.296	0.801	−0.287
Δ_γ	0.978	−0.111	2.085	−0.153	0.857	−0.155
$\lvert\Delta\rvert_{xyz}$	0.992	0.170	0.909	0.315	0.982	0.236
$\lvert\Delta\rvert_{\alpha\beta\gamma}$	0.935	0.322	1.087	0.160	1.020	0.260

The numerical values of variances for the F/D fit are far greater than the D/F fit. In the D/F experiment, it was possible to obtain resulting forces/moments in all 6DoF. A torsional load along the diagonal vector of the MP frame is the only load type that is not generated. The F/D setup has a single direction force and moment loading. Also, the weight of the links is relatively equally distributed on all bodies. Thus, the F/D experiment has a limited loading diversity. Therefore, links did not experience some forces/moments types. As a result, the weight parameters corresponding to the stiffness of those frames have no role in scaling the stiffness value, and their variance is high.

The computed weights show higher variance in W_1, W_2, W_3, W_4, W_7, and W_8. Due to different test conditions of HISS, it is hard to find a correlation for the fitting algorithm between D/F and F/D results. The contact force of CMM's probe may change the applied load condition in the F/D setup. Hence, the model fitting algorithm struggles to converge the parameters to a constant, and the fitting algorithm prefers to focus on modifying the last links of a serial chain. A change in the stiffness of this link directly affects the compliance without any consideration of kinematics since it is closer to the MP. The fitting algorithm increases the stiffness of the first two links and tries to solve the problem by modifying the last links and suppresses the kinematic relations.

5.2 Stiffness Model Fitting and Fine-Tuning. Figure 10 shows the top 15 largest and smallest errors for the norms of translational and rotational deflections between fine-tuned model outputs. The results are sorted with respect to measurement data in ascending order to easily observe the performance of the model and fine-tuning operation. The error data are computed by subtracting the experiment data from the fitted model and fine-tuned model.

Two levels of the fine-tuning processes are conducted. First, directional deflections and rotations are fine-tuned individually. Then, the norms of fine-tuned translational and rotational deflections are computed. Second, correction functions are acquired for the computed norm data. Linear correction functions are adopted for fine-tuning. The parameters of correction functions and their performance are given in Tables 3 and 4, respectively.

The translational stiffness performance of the models is investigated for all three types of data sets. In the top 15 largest translation errors for D/F results, the error ranges between $\sim\pm1$ mm for both fitted and fine-tuned models. Similar behavior is also observed in F/D fitting results, but the error increases up to 2 mm for the combined dataset of D/F + F/D. Among all 15 errors, TP4 is observed four times in the largest error family of D/F results. Three occurrences of TP9 and TP10 are recorded for the same error family of F/D. The combined dataset results to have four occurrences of TP4 and TP8.

The larger dataset of combined data should provide a better model due to diversity and a high number of data. However, maximum error, RMS error, standard deviation, and absolute mean (AM) error of the combined dataset are higher compared to D/F and F/D results. Since the test conditions of the manipulator are different in both D/F and F/D experiments, there is less correlation between the experiments. Thus, combined data adversely affect the fitting algorithm.

The mean error of the top 15 smallest translational errors is 0 mm and there is no noticeable variance for fine-tuned model results. With four occurrences, TP3 is the best performing test point in D/F results. Three occurrences of TP3, TP6, and again, four occurrences of TP3 are observed among the smallest translational error of F/D and D/F + F/D results, respectively.

Although TP3 is the most compliant pose of the HISS manipulator, it produces the minimum errors. There are three main reasons for this outcome. First, TP3 is a fully isotropic pose in terms of stiffness behavior. Second, the precision of the CMM is less important when the measurements are large. Third, model fitting and fine-tuning algorithms mainly focus on larger deflections to decrease the error since the large deflections are more sensitive to model parameters. As a result, the top 15 largest deflection errors are observed up to 4.5 mm MP deflection range while the smallest errors can be computed up to 6 mm deflections.

When the top 15 largest rotational errors of all types of data sets are considered, both the model fitting and the fine-tuning fail to follow the increasing trend of the measurements. The rotational errors range between $\sim\pm1$ deg, however, measurements can reach up to 2 deg rotations. Interestingly, the largest rotational errors of the fine-tuned model are observed when the measurement is closed to 0 deg and the fitted model produces less error. Fine-tuning decreases the error in large rotational deflection regions since the correction function mostly shifts upward the results. This effect is more apparent in the top 15 smallest rotational error plots of D/F and F/D. Fine-tuning increases the model performance and decreases RMS error, the standard deviation of the error, and absolute mean error for D/F and F/D. Fine-tuning in the combined dataset has no significant contribution. RMS error and standard deviation remain roughly the same and the mean error still decreased to 0, but the absolute mean error increased.

Table 4 Statistic evaluations of the models, root mean squared (RMS), standard deviation (Std), mean (*M*), absolute mean (AM)

	D/F								F/D								F/D + D/F							
	Fitted model				Fine-tuned model				Fitted model				Fine-tuned model				Fitted model				Fine-tuned model			
	RMS	Std	*M*	AM	RMS	Std	*M*	AM	RMS	Std	*M*	AM	RMS	Std	*M*	AM	RMS	Std	*M*	AM	RMS	Std	*M*	AM
Δ_x	0.64	0.65	−0.04	0.42	0.61	0.62	0	0.39	0.41	0.41	−0.09	0.30	0.40	0.41	0	0.30	0.74	0.74	0.04	0.50	0.65	0.66	0	0.45
Δ_y	0.63	0.52	0.37	0.49	0.51	0.52	0	0.41	0.60	0.57	0.21	0.47	0.56	0.57	0	0.45	0.71	0.64	0.31	0.55	0.62	0.62	0	0.47
Δ_z	0.43	0.43	−0.03	0.31	0.38	0.38	0	0.28	0.49	0.43	−0.25	0.37	0.39	0.39	0	0.31	0.59	0.59	−0.09	0.44	0.49	0.50	0	0.38
Δ_α	0.59	0.49	−0.33	0.44	0.49	0.49	0	0.35	0.38	0.37	−0.12	0.30	0.35	0.35	0	0.26	0.54	0.52	−0.16	0.41	0.48	0.48	0	0.37
Δ_β	0.56	0.53	0.19	0.44	0.52	0.53	0	0.45	0.50	0.42	0.27	0.40	0.41	0.42	0	0.36	0.62	0.54	0.32	0.51	0.52	0.52	0	0.45
Δ_γ	0.43	0.42	0.11	0.33	0.41	0.42	0	0.31	0.38	0.37	0.08	0.25	0.32	0.33	0	0.23	0.48	0.44	0.19	0.37	0.43	0.43	0	0.32
$\lvert\Delta\rvert_{xyz}$	0.45	0.45	0.04	0.36	0.35	0.35	0	0.27	0.45	0.44	−0.13	0.33	0.41	0.42	0	0.32	0.64	0.63	0.12	0.51	0.50	0.50	0	0.38
$\lvert\Delta\rvert_{\alpha\beta\gamma}$	0.47	0.37	−0.30	0.39	0.33	0.34	0	0.27	0.53	0.40	−0.35	0.41	0.40	0.41	0	0.32	0.42	0.41	−0.08	0.32	0.41	0.41	0	0.33

6 Discussion and Conclusion

In this study, a methodology for stiffness model fitting to the experimental data and a fine-tuning are proposed. HISS haptic device is investigated as a master controller of surgical robots. Two experiment setups are introduced. In the first setup, six degrees-of-freedom compliant displacements are applied on the mobile platform of the HISS and the reaction loads are captured. This setup lacks capturing contribution of the link weights on compliance and possible joint clearances. In the second test setup, single-axis loads are applied to address the problems of the first one. However, applied load types are very limited with respect to the first test setup and the contact force of CMM's probe affects the measurements. The model fitting procedure scales the stiffness of the links to comply with the experiment data while a linear correction function modifies the model outputs for fine-tuning.

When the first and the second test setup results are separately used in model fitting, the translational deflection outputs of the model capture the general nonlinear stiffness behavior of the experiment. The stiffness model fitted to the first experiment results performs better since a larger dataset is used. It is hard to predict the outputs of the stiffness model of the second experiment when a different type of load is applied because of the limited load types. When all experiment data are combined for model fitting, the overall performance of the stiffness model is reduced. Therefore, it is better to use the same experimental setup and apply different kinds of load/displacement conditions. Finally, the results obtained for the rotational deflections are not as accurate as the ones received for the translational deflection results. This problem can be solved by considering separately translational and rotational deflections.

Acknowledgment

We thank Mr. Barış Taner, Mr. Erkan Paksoy and Mr. Uğur Nalbant for their contributions to the manufacturing of experiment setup and Ms. Hazal Emet and Mr. Uğur Nalbant for conducting experiments.

Funding Data

- Izmir Yüksek Teknoloji Enstitüsü (No. 2016IYTE49; Funder ID: 10.13039/501100003984).
- Türkiye Bilimsel ve Teknolojik Araştirma Kurumu (No. 117M405; Funder ID: 10.13039/501100004410).

Appendix: Stiffness Matrices of the Links

Upper left, upper right, lower left, and lower right 3×3 submatrices have the units of N/m, N/rad, N/rad, and N·m, respectively,

$$\mathbf{K}_{\theta 1} = \begin{bmatrix} 415,799,028 & 0 & 0 & 0 & 0 & 0 \\ 0 & 7,680,832 & 0 & 0 & 0 & -470,067 \\ 0 & 0 & 7,680,832 & 0 & 470,067 & 0 \\ 0 & 0 & 0 & 7376 & 0 & 0 \\ 0 & 0 & 470,067 & 0 & 38,357 & 0 \\ 0 & -470,067 & 0 & 0 & 0 & 38,357 \end{bmatrix} \tag{A1}$$

$$\mathbf{K}_{\theta 2} = \begin{bmatrix} 104,295,294 & 531,064 & 0 & 0 & 0 & -39,116 \\ 531,064 & 1,257,978 & 0 & 0 & 0 & -50,789 \\ 0 & 0 & 8,203,161 & 13,292 & 296,364 & 0 \\ 0 & 0 & 13,292 & 884 & 480 & 0 \\ 0 & 0 & 296,364 & 480 & 23,175 & 0 \\ -39,116 & -50,789 & 0 & 0 & 0 & 2655 \end{bmatrix} \tag{A2}$$

$$\mathbf{K}_{\theta 3} = \begin{bmatrix} 174,532,925 & 0 & 0 & 0 & 0 & 0 \\ 0 & 1,278,122 & 0 & 0 & 0 & -82,822 \\ 0 & 0 & 1,278,122 & 0 & 82,822 & 0 \\ 0 & 0 & 0 & 1376 & 0 & 0 \\ 0 & 0 & 82,822 & 0 & 7156 & 0 \\ 0 & -82,822 & 0 & 0 & 0 & 7156 \end{bmatrix} \tag{A3}$$

References

[1] Zahiri, M., Booton, R., Siu, K.-C., and Nelson, C. A., 2017, "Design and Evaluation of a Portable Laparoscopic Training System Using Virtual Reality," ASME J. Med. Devices, **11**(1), p. 011002.

[2] Prince, S. W., Kang, C., Simonelli, J., Lee, Y.-H., Gerber, M. J., Lim, C., Chu, K., Dutson, E. P., and Tsao, T.-C., 2020, "A Robotic System for Telementoring and Training in Laparoscopic Surgery," Int. J. Med. Rob. Comput. Assisted Surg., **16**(2), p. e2040.

[3] Lim, J. H., Lee, W. J., Park, D. W., Yea, H. J., Kim, S. H., and Kang, C. M., 2017, "Robotic Cholecystectomy Using Revo-i Model MSR-5000, the Newly Developed Korean Robotic Surgical System: A Preclinical Study," Surg. Endoscopy, **31**(8), pp. 3391–3397.

[4] D'Auria, D., and Persia, F., 2017, "A Collaborative Robotic Cyber Physical System for Surgery Applications," IEEE International Conference on Information Reuse and Integration (IRI), San Diego, CA, Aug. 4–6, pp. 79–83.

[5] Palep, J. H., 2009, "Robotic Assisted Minimally Invasive Surgery," J. Minimal Access Surg., **5**(1), p. 1.

[6] Chapman, W. H. H., Albrecht, R. J., Kim, V. B., Young, J. A., and Chitwood, W. R., 2002, "Computer-Assisted Laparoscopic Splenectomy With the da Vinci™ Surgical Robot," J. Laparoendosc. Adv. Surg. Tech., **12**(3), pp. 155–159.

[7] Antonakoglou, K., Xu, X., Steinbach, E., Mahmoodi, T., and Dohler, M., 2018, "Toward Haptic Communications Over the 5G Tactile Internet," IEEE Commun. Surv. Tutorials, **20**(4), pp. 3034–3059.

[8] Simsek, M., Aijaz, A., Dohler, M., Sachs, J., and Fettweis, G., 2016, "5G-Enabled Tactile Internet," IEEE J. Sel. Areas Commun., **34**(3), pp. 460–473.

[9] Tholey, G., and Desai, J. P., 2008, "A Compact and Modular Laparoscopic Grasper With Tridirectional Force Measurement Capability," ASME J. Med. Devices, **2**(3), p. 031001.
[10] Talasaz, A., Luisa Trejos, A., Perreault, S., Bassan, H., and Patel, R. V., 2014, "A Dual-Arm 7-Degrees-of-Freedom Haptics-Enabled Teleoperation Test Bed for Minimally Invasive Surgery," ASME J. Med. Devices, **8**(4), p. 041004.
[11] Carbone, G., 2013, "Stiffness Analysis for Grasping Tasks," *Grasping in Robotics*, Springer, Dordrecht, The Netherlands, pp. 17–55.
[12] Mahvash, M., and Dupont, P. E., 2011, "Stiffness Control of Surgical Continuum Manipulators," IEEE Trans. Rob., **27**(2), pp. 334–345.
[13] Mattos, L. S., Caldwell, D. G., Peretti, G., Mora, F., Guastini, L., and Cingolani, R., 2016, "Microsurgery Robots: Addressing the Needs of High-Precision Surgical Interventions," Swiss Med. Wkly., **146**(4344), p. w14375.
[14] Mekaouche, A., Chapelle, F., and Balandraud, X., 2015, "FEM-Based Generation of Stiffness Maps," IEEE Trans. Rob., **31**(1), pp. 217–222.
[15] Pashkevich, A., Chablat, D., and Wenger, P., 2009, "Stiffness Analysis of Overconstrained Parallel Manipulators," Mech. Mach. Theory, **44**(5), pp. 966–982.
[16] Júnior, G. S., Carvalho, J. C. M., and Gonçalves, R. S., 2016, "Stiffness Analysis of Multibody Systems Using Matrix Structural Analysis-MSA," Robotica, **34**(10), pp. 2368–2385.
[17] Klimchik, A., Pashkevich, A., and Chablat, D., 2019, "Fundamentals of Manipulator Stiffness Modeling Using Matrix Structural Analysis," Mech. Mach. Theory, **133**, pp. 365–394.
[18] Görgülü, İ., Carbone, G., and Dede, M. C., 2020, "Time Efficient Stiffness Model Computation for a Parallel Haptic Mechanism Via the Virtual Joint Method," Mech. Mach. Theory, **143**, p. 103614.
[19] Yu, G., Wang, L., Wu, J., Wang, D., and Hu, C., 2018, "Stiffness Modeling Approach for a 3-DOF Parallel Manipulator With Consideration of Nonlinear Joint Stiffness," Mech. Mach. Theory, **123**, pp. 137–152.
[20] Carbone, G., 2011, "Stiffness Analysis and Experimental Validation of Robotic Systems," Front. Mech. Eng., **6**(2), pp. 182–196.
[21] Wu, Y., Klimchik, A., Caro, S., Boutolleau, C., Furet, B., and Pashkevich, A., 2014, "Experimental Study on Geometric and Elastostatic Calibration of Industrial Robot for Milling Application," IEEE/ASME International Conference on Advanced Intelligent Mechatronics, Besancon, France, July 8–11, pp. 1689–1696.
[22] Klimchik, A., Ambiehl, A., Garnier, S., Furet, B., and Pashkevich, A., 2016, "Experimental Study of Robotic-Based Machining," IFAC-PapersOnLine, **49**(12), pp. 174–179.
[23] Klimchik, A., Magid, E., and Pashkevich, A., 2016, "Design of Experiments for Elastostatic Calibration of Heavy Industrial Robots With Kinematic Parallelogram and Gravity Compensator," IFAC-PapersOnLine, **49**(12), pp. 967–972.
[24] Lian, B., Sun, T., Song, Y., Jin, Y., and Price, M., 2015, "Stiffness Analysis and Experiment of a Novel 5-DOF Parallel Kinematic Machine Considering Gravitational Effects," Int. J. Mach. Tools Manuf., **95**, pp. 82–96.
[25] Sun, T., Wu, H., Lian, B., Qi, Y., Wang, P., and Song, Y., 2017, "Stiffness Modeling, Analysis and Evaluation of a 5 Degree of Freedom Hybrid Manipulator for Friction Stir Welding," Proc. Inst. Mech. Eng., Part C, **231**(23), pp. 4441–4456.
[26] Taner, B., and Dede, M. I. C., 2017, "Image Processing Based Stiffness Mapping of a Haptic Device," *New Advances in Mechanisms, Mechanical Transmissions and Robotics*, Springer, Dordrecht, The Netherlands, pp. 447–454.
[27] Švaco, M., Šekoranja, B., Šuligoj, F., and Jerbić, B., 2014, "Calibration of an Industrial Robot Using a Stereo Vision System," Procedia Eng., **69**, pp. 459–463.
[28] Gonzalez-Hernandez, A., and Castillo-Castaneda, E., 2013, "Stiffness Estimation of a Parallel Manipulator Using Image Analysis and Camera Calibration Techniques," Robotica, **31**(4), pp. 657–667.
[29] Görgülü, İ., Dede, M. C., and Carbone, G., 2019, "An Experimental Test Procedure for Validation of Stiffness Model: A Case Study for R-Cube Parallel Mechanism," IFToMM International Symposium on Robotics and Mechatronics, Taipei, Taiwan, Springer, pp. 391–402.
[30] Slavković, N. R., Milutinović, D. S., Kokotović, B. M., Glavonjić, M. M., Živanović, S. T., and Ehmann, K. F., 2013, "Cartesian Compliance Identification and Analysis of an Articulated Machining Robot," FME Trans., **41**(2), pp. 83–95.
[31] Hernández-Martínez, E. E., Ceccarelli, M., Carbone, G., López-Cajún, C. S., and Jáuregui-Correa, J. C., 2010, "Characterization of a Cable-Based Parallel Mechanism for Measurement Purposes," Mech. Based Des. Struct. Mach., **38**(1), pp. 25–49.
[32] Yan, S., Ong, S., and Nee, A., 2016, "Stiffness Analysis of Parallelogram-Type Parallel Manipulators Using a Strain Energy Method," Rob. Comput.-Integr. Manuf., **37**, pp. 13–22.
[33] Dumas, C., Caro, S., Chérif, M., Garnier, S., and Furet, B., 2010, "A Methodology for Joint Stiffness Identification of Serial Robots," IEEE/RSJ International Conference on Intelligent Robots and Systems, Taipei, Taiwan, Oct. 18–22, pp. 464–469.
[34] Ding, B., Cazzolato, B. S., Stanley, R. M., Grainger, S., and Costi, J. J., 2014, "Stiffness Analysis and Control of a Stewart Platform-Based Manipulator With Decoupled Sensor–Actuator Locations for Ultrahigh Accuracy Positioning Under Large External Loads," ASME J. Dyn. Syst., Meas., Control, **136**(6), p. 061008.
[35] Nyce, D. S., 2016, *Position Sensors*, Wiley, Hoboken, NJ.
[36] Görgülü, İ., 2018, "Optimal Design of a Kinesthetic Haptic Device Mechanism for Enhancing Its Impedance Characteristics," Master's thesis, Izmir Institute of Technology, Izmir, Turkey.
[37] Li, W., Gao, F., and Zhang, J., 2005, "R-Cube, a Decoupled Parallel Manipulator Only With Revolute Joints," Mech. Mach. Theory, **40**(4), pp. 467–473.
[38] Klimchik, A., 2011, "Enhanced Stiffness Modeling of Serial and Parallel Manipulators for Robotic-Based Processing of High Performance Materials," Ph.D. thesis, Ecole Centrale de Nantes (ECN); Ecole des Mines de Nantes, Nantes, France.
[39] Kern, T. A., 2009, *Engineering Haptic Devices: A Beginner's Guide for Engineers*, Springer Publishing Company, London, UK.